Journal of
Low Power Electronics and Applications

MDPI

Article

Advanced Modelling and Performance Analysis of a Separately Excited Direct-Current Motor Powered by Photovoltaic Generators Using Maximum Power Point Tracking Techniques

Feras Alasali [1], Tha'er O. Sweidan [2], Mohammed I. Abuashour [1] and William Holderbaum [3,*]

[1] Department of Electrical Engineering, Faculty of Engineering, The Hashemite University, Zarqa 13133, Jordan; ferasasali@hu.edu.jo (F.A.); mohammedi@hu.edu.jo (M.I.A.)
[2] Faculty of Engineering Technology and Science, Higher Colleges of Technology, Sharjah 7947, United Arab Emirates; tsweidan@hct.ac.ae
[3] Department of Biomedical Sciences and Biomedical Engineering, School of Biological Sciences, University of Reading, Reading RG6 7BE, Berkshire, UK
* Correspondence: w.holderbaum@reading.ac.uk

Abstract: The integration of photovoltaic (PV) systems into DC motor drives has prompted the enhancement of motor performance. This study explores the application of photovoltaic generators (PVs) to independently power and excite a Separately Excited Direct-Current (SEDC) system by utilizing a proportional open-circuit voltage method as a strategy for tracking the maximum power point. This approach offers an effective means of optimizing energy output from PV systems. The primary aim was to optimize power output from photovoltaic generators across varying solar intensity levels. This paper describes the nonlinear current/voltage behaviour of PV generators under different levels of irradiation, along with the magnetic characteristics of the core material in an SEDC motor, utilizing advanced polynomial equations for accurate mathematical representation. Furthermore, we conducted a dynamic analysis of the SEDC motor, powered by the PV generators, under varying solar intensities. This study investigates the operational performance of the SEDC motor under varying solar irradiance levels by developing a realistic model using MATLAB software, R2022a, for numerical simulations, followed by implementation on high-performance computing platforms, including a real-time simulator and testbed, using a real-time digital simulator (RTDS).

Keywords: SEDC motor; maximum power point tracking; PV generator; real-time digital simulator; steady-state analysis

Citation: Alasali, F.; Sweidan, T.O.; Abuashour, M.I.; Holderbaum, W. Advanced Modelling and Performance Analysis of a Separately Excited Direct-Current Motor Powered by Photovoltaic Generators Using Maximum Power Point Tracking Techniques. *J. Low Power Electron. Appl.* **2024**, *14*, 56. https://doi.org/10.3390/jlpea14040056

Academic Editor: Pak Kwong Chan

Received: 28 October 2024
Revised: 24 November 2024
Accepted: 25 November 2024
Published: 28 November 2024

1. Introduction

1.1. Background

Recent advancements in power electronics and modern semiconductor technologies have facilitated the emergence of various electric drive systems. DC motors, in particular, have found extensive applications in both industrial environments and smart hybrid solutions. The increasing availability of solar energy, recognized for its eco-friendly benefits, offers a promising avenue to investigate standalone or grid-connected photovoltaic (PV) power sources for DC motor drives. This shift towards PV systems has stimulated new research focused on enhancing motor performance [1–3]. To maximize power extraction from PV generators, the implementation of Maximum Power Point Tracking (MPPT) techniques is essential. Numerous studies have explored a range of MPPT algorithms and control strategies aimed at optimizing PV system performance, particularly in conjunction with electric motors [4–6]. For instance, one study examined the dynamical and steady-state performance of DC series motors and induction motors powered by a photovoltaic (PV) generator under varying solar irradiance levels. The maximum power point of the PV generator's current/voltage (I/V) characteristics is achieved using the open-circuit voltage

method. To model the nonlinear behaviour of the PV generator's I/V characteristics and the magnetization curve of the DC series motor, high-order polynomial mathematical expressions are used. This study examines the response of these motors at different solar intensities and evaluates their performance under step changes in solar irradiance with a fixed load torque. Numerical simulations are carried out using MATLAB software, providing insights into how solar intensity variations impact motor operation [7].

1.2. Literature Review

A fuzzy logic controller (FLC) framework has been developed to optimize power extraction from a standalone PV system within a water-pumping application. This system integrates a DC-DC buck chopper with a fuzzy MPPT, which continuously adjusts the duty cycle of the buck converter to maintain optimal impedance matching with the PV panel, ensuring maximum power transfer efficiency. The main objective is to improve both motor speed and water output from the centrifugal pump. Simulation results using MATLAB/Simulink (version 9.1) show that the FLC outperforms a system where the PV generator is directly connected to the pump, particularly under varying sunlight conditions [8]. Furthermore, the study also modelled and formulated a control strategy for a grid-connected wind–PV hybrid system. Simulation results demonstrated that the system could produce synchronized sinusoidal current waveforms while maintaining a steady DC bus voltage by injecting active power into the grid, thereby confirming its operational efficiency [9]. This study compared three techniques for maximizing power transfer from a PV generator: incremental conductance, hill climbing, and perturbation and observation. The study highlights that factors such as temperature, solar irradiation, and load conditions affect the operating point of the PV generator, necessitating load adaptation for optimal power transfer. This is accomplished using a step-up DC-DC converter controlled by an MPPT algorithm. Simulations showed that these techniques efficiently track maximum power, aligning closely with the manufacturer's specifications for the PV system under various conditions. A detailed study [10] on energy transformation in wind power systems emphasized the importance of selecting suitable topologies to enhance performance, efficiency, and reliability. Another paper [11] also underlined the significance of MPPT in energy harvesting and reviewed various energy conversion topologies, their advantages, disadvantages, and applications. The research provided a comprehensive analysis, making it an essential resource for researchers and engineers in the field of energy conversion [11]. This study proposed an optimization strategy for a PV water-pumping system using MPPT, focusing on achieving maximum power output by adjusting the duty cycle of a buck–boost converter. A dynamic controller using a nonlinear autoregressive moving average model integrated with neural networks was implemented to enhance the duty cycle. Simulation results demonstrated accurate MPPT, and the neural network (NN) controller outperformed a proportional–integral–derivative (PID) controller, showing clear advantages [12]. In a following study, a voltage-based MPPT technique was introduced that avoids the limitations of the constant voltage method, which traditionally requires disconnecting the PV panel from the load to measure the open-circuit voltage. The authors proposed using a pilot PV panel for this measurement and incorporated a proportional–integral (PI) controller, modelled in MATLAB® /Simulink. Simulation results confirmed that this new method significantly improved system efficiency [13]. The study analyzed the Perturbation and Observation (P&O) method for MPPT in a grid-connected PV generation system. Large-signal stability analysis was performed for a balanced three-phase to-ground fault under varying levels of solar irradiance. The results demonstrated that the system maintained stability during significant disturbances and fluctuations in solar irradiance, with higher irradiance leading to longer fault-clearing times and reduced settling times [14]. The P&O algorithm for MPPT in a PV-powered DC shunt motor was further explored, adapting the PV generator's operating point to achieve optimal power under changing solar conditions. Additionally, the study analyzed a standalone wind/PV hybrid system for pumping and a PV array powering a three-phase motor driving a centrifugal pump.

MATLAB simulations confirmed effective operation under varying solar intensities and motor loads [15].

An examination study [16] was conducted on a dual-source brushless DC motor drive system powered by a solar PV array and the grid. The system integrated a boost DC-DC converter utilizing an incremental conductance algorithm for MPP tracking and a bridgeless asymmetrical converter designed to enhance power quality and minimize component requirements. Performance was rigorously analyzed under scenarios including solar-only, grid-only, and hybrid operation. Stability was verified using Bode diagrams and pole–zero plots. Simulations in MATLAB/Simulink demonstrated the system's high efficiency and reliability [16]. Additionally, this research explored strategies to optimize power utilization in electric vehicles employing Proton-Exchange Membrane Fuel Cells (PEMFCs). Among the evaluated methods, the Adaptive Step Value with a Cuckoo Search Algorithm (ASV-CSA) proved to be the most effective, offering superior performance in terms of speed and stability for extracting maximum power [17]. Another study proposed a PV water-pumping system as an environmentally friendly alternative to diesel-powered irrigation pumps. This system incorporated a PV emulator, a boost converter with MPPT, and a motor pump emulator. Validation through both simulations and experimental testing confirmed its high performance, rapid response to solar fluctuations, and precise replication of PV characteristics, positioning it as a sustainable and reliable solution for irrigation [18]. In another research study [19], the authors proposed an innovative control strategy for Photovoltaic Water-Pumping Systems (PV-WPSs) by integrating Sliding Mode Control (SMC) with MPPT techniques. The approach achieved 70% enhancement in water flow rates compared to systems lacking MPPT capabilities. It demonstrated robust performance against environmental variations, making it a viable option for off-grid water supply applications [19]. A separate study introduced a speed regulation mechanism for an SEDC motor utilizing a chopper circuit. The design incorporated a PI controller to ensure rapid and precise response without delays. MATLAB/Simulink simulations validated the effectiveness of this chopper-based approach in maintaining motor speed under diverse operating conditions [20]. Additionally, another study presented a Particle Swarm Optimization (PSO) algorithm aimed at fine-tuning the scaling factors of a fuzzy PID controller for nonlinear systems, such as DC motors. The PSO-optimized fuzzy PID controller outperformed traditional methods, including the Ziegler–Nichols technique, particularly in disturbance rejection and trajectory tracking. These improvements were corroborated through simulations conducted in MATLAB/Simulink [21].

As presented in Table 1, this literature review presents important insights into various motor drives that integrate MPPT techniques and control strategies, as well as comparative studies aimed at optimizing the performance of PV systems, particularly DC motors. Despite these advancements, there are still knowledge gaps in understanding the dynamic interactions between PV generators and separately excited DC motors, especially in real-world operational scenarios. While significant advancements have been made in the integration of MPPT techniques and control strategies for optimizing PV system performance, several knowledge gaps remain. These include a limited understanding of the dynamic interactions between PV generators and separately excited DC motors under varying environmental conditions, especially in real-world applications. Additionally, there is a need for more robust and adaptive control strategies that can handle uncertainties in system parameters and external disturbances, such as varying solar irradiance and motor load fluctuations. Furthermore, existing research often focuses on individual components of the PV system, without thoroughly addressing the interactions between the PV source, MPPT controller, and motor drive system in a unified framework. This research aims to bridge these gaps by providing an advanced modelling and performance analysis of a separately excited DC motor powered by PV generators, utilizing MPPT techniques to optimize system performance across a range of real-world conditions. This study will also explore the integration of control algorithms to improve the overall stability and efficiency of the system, contributing to more reliable and sustainable PV-powered motor drives.

Table 1. Comprehensive overview of recent advances in DC motors with MPPT techniques.

Reference	Authors	Problem Addressed	Proposed Solution
[1]	Frikha et al. (2023)	Challenges in multiphase motor and drive systems for EVs	Explored cutting-edge advancements and predicted future trends in EV powertrains
[2]	Rafin et al. (2023)	Advancements in power electronics using wide and ultrawide bandgap devices	Provided a thorough evaluation of emerging power electronics technologies
[3]	Ze Wang et al. (2024)	Torque overload in motor drives with energy storage systems	Developed a hybrid energy storage and management framework
[4]	Katche et al. (2023)	Maximizing PV system efficiency through MPPT	Conducted an in-depth review of advanced MPPT methods
[5]	Kandemir et al. (2017)	Extracting peak power from PV systems	Reviewed state-of-the-art MPPT techniques for higher efficiency
[6]	Lyu et al. (2024)	Enhancing MPPT algorithms for PV applications	Utilized numerical methods for performance improvement in MPPT
[7]	Abuashour et al. (2019)	Dynamic performance analysis of PV-powered DC motors	Used FOCV MPPT to evaluate motor responses under different conditions
[8]	Aashoor & Robinson (2013)	Improving PV water pumping with MPPT	Implemented fuzzy-logic-based MPPT for superior tracking performance
[9]	Laabidi & Mami (2015)	Hybrid systems combining wind and PV energy	Devised control mechanisms for optimized wind/PV integration
[10]	El Hassouni et al. (2018)	Boosting MPPT efficiency in PV systems	Evaluated MPPT with boost converters for high efficiency
[11]	Mansouri et al. (2023)	Wind energy conversion challenges with MPPT	Conducted a review of MPPT techniques tailored for wind systems
[12]	Kassem (2011)	Controlling PV-powered motor pump systems	Proposed neural-network-based MPPT for enhanced control
[13]	Asim et al. (2016)	Limitations of constant voltage-based MPPT	Developed an improved MPPT approach for PMDC motor applications
[14]	Sweidan et al. (2019)	Stability concerns in grid-connected PV systems	Used P&O MPPT for large-signal stability evaluation
[15]	Abuashour et al. (2018)	Performance of hybrid wind/PV systems for pumping	Assessed hybrid energy systems through modelling and simulations
[16]	Shukla & Nikolovski (2022)	PV/grid hybrid systems for water pumping	Designed a system using brushless DC motors for efficient operation
[17]	Eswaraiah & Balakrishna (2024)	Adaptive MPPT controllers for renewable systems	Developed and analyzed advanced adaptive MPPT controllers
[18]	Fatah et al. (2024)	PV system emulation for water pumping	Introduced a PV emulator with dynamic analysis and hardware validation
[19]	Farhat & Barambones (2024)	Optimizing standalone PV water-pumping systems	Proposed advanced optimization strategies for off-grid solutions
[20]	Al Mashhadany et al. (2023)	Speed regulation in DC motors using chopper circuits	Integrated high-performance control for precise motor speed management
[21]	Wubu et al. (2024)	Speed tracking in DC motors	Developed a PSO-optimized fuzzy PID controller for improved tracking accuracy
[22]	Sridhar et al. (2015)	Multilevel inverters in PV systems	Analyzed cascaded inverter configurations for reduced switch counts
[23]	Patel (1999)	Integration of wind and solar energy systems	Offered a comprehensive guide to hybrid system integration techniques
[24]	Ong (1998)	Dynamic simulation in electric machinery	Explored dynamic behaviour through simulation techniques

Table 1. *Cont.*

Reference	Authors	Problem Addressed	Proposed Solution
[25]	Jain & Agarwal (2007)	MPPT in grid-tied PV systems	Compared MPPT schemes for grid-connected PV applications
[26]	Mohan & Undel (2007)	Power electronics in renewable systems	Highlighted applications and challenges in renewable power electronics
[27]	Abu-Siada & Islam (2024)	Distributed energy integration with power electronics	Addressed the integration challenges of distributed energy resources
[28]	Eldali (2024)	Distributed energy systems and power electronics	Explored advanced electronics for seamless energy resource integration
[29]	Kolhe et al. (2004)	Performance of PV-powered water-pumping systems	Evaluated performance metrics for directly coupled systems
[30]	Antonio & Luis (2021)	PV-powered DC motor control	Developed FPGA-based control for enhanced disturbance rejection

1.3. Contributions

This proposed work focuses on the development and simulations of a DC motor drive system that is fed from a photovoltaic panel. This photovoltaic-powered DC motor system has numerous vital industrial applications, such as air fans in large spaces, air circulation in green homes that remove unhealthy air from confined areas, and irrigation in rural areas. When photovoltaic power is to be used for a DC motor, which will typically serve the purpose of variable speed drives, various schemes are available in the literature. The proposed method employs a separately excited DC motor that is powered by two PV generators that supply the motor's armature and field circuits. This work utilizes a fractional open-circuit voltage technique to achieve maximum power for PVs. By dynamically adjusting the duty cycle, the output voltage of the converter is regulated to match the voltage at the maximum power. This ensures optimal power delivery to the motor's circuits, maximizing efficiency and performance. In addition, this work investigates the performance of a DC separately excited motor as it responds to varying levels of solar irradiance by designing a realistic model using high-performance computing, real-time simulator, and testbed, using RTDS. The analysis includes examining steady-state output characteristics and highlighting how changes in solar energy input influence the motor's efficiency, torque, and operational stability. Various irradiance conditions will be simulated to assess the motor's adaptability and effectiveness in harnessing solar energy.

The objectives of this study encompass designing and implementing a control system tailored for a separately excited DC motor, which is powered by two PV generators. Additionally, the performance of the proposed system is analyzed in terms of efficiency, stability, and response time. The novelty of this system is that, firstly, it introduces the application of a proportional open-circuit voltage method as a strategy for tracking the maximum power point in PVs. While the open-circuit voltage method is a well-established technique for determining the maximum power point, its application in the dual PV configuration with a separately excited DC motor is not commonly explored. This unique setup addresses the nonlinear interactions between the motor's field and armature circuits, enhancing both power delivery and system stability. Secondly, it integrates two PV generators to jointly power a single DC motor. Thirdly, the control strategy employed involves adjusting the duty cycle of the converter to accurately track the maximum power. A comprehensive performance evaluation of the proposed system has been conducted to assess its efficiency, stability, and response time, thereby providing insights into its practical applicability and effectiveness.

1.4. Paper Structure

This work is structured as follows: Section 2 describes the configuration of the system under investigation and provides details regarding the designed PV generator, the mathematical model describing the dynamical behaviour of the DC separately excited motor, the DC-DC buck–boost converters, and the MPPT controllers. Section 3 presents the results of numerical simulations and subsequent discussions. Finally, Section 4 summarizes the conclusions drawn from this study.

2. Methodological Framework

This section provides a detailed examination of the system configuration and the various components central to our study. It outlines the integration of photovoltaic (PV) systems that drive an SEDC motor, with a focus on the design considerations for the PV generators. Additionally, it describes the dynamic modelling of the entire system to the SEDC motor. The proposed method is adaptable and can be implemented in various practical applications, including agricultural irrigation systems where reliable water pumping is essential and greenhouse ventilation systems that require consistent power for temperature and humidity control. Its modular design supports scalability, allowing it to be adapted for larger systems, such as industrial motors, while maintaining efficient energy use. Additionally, the system's compatibility with hybrid energy configurations, including solar and wind power integration, enhances its functionality for remote-area power supplies where access to the grid is limited. These features make the method a robust and adaptable solution for addressing diverse energy needs in sustainable and off-grid energy applications.

2.1. System Setup and Details

Figure 1 presents a schematic representation of a standalone PV system that powers an SEDC motor. The configuration of the PV generators involves connecting several modules in both series and parallel arrangements to meet the required specifications for the armature and field of the SEDC motor. An intermediate component, a DC-DC converter, is positioned between the PVs and the armature, as well as between the PV generator and the field of the SEDC motor. This converter is responsible for regulating the output voltage to facilitate tracking. The converter is specifically employed to deliver voltage at the maximum power of the system, ensuring optimal energy extraction from the PV source. This voltage then supplies both the armature and the field circuits of the SEDC motor by adjusting its duty cycle as needed. In this work, MATLAB and RTDS were used as simulation platforms due to their robust capabilities in modelling and simulating power electronic systems and renewable energy technologies. RTDS is a high-performance real-time computing platform. The RTDS No-vaCore 2.0, the latest generation of its central processing hardware, serves as the foundational unit for real-time digital simulation. MATLAB's extensive toolboxes, particularly for power electronics and control systems, enable detailed analysis. Additionally, MATLAB's Simulink component simplifies the modelling of nonlinear systems, such as PV-powered DC motors, by providing a user-friendly interface with pre-built blocks and advanced customization options. The simulations were conducted in intervals, which allowed for capturing transient behaviours effectively over a simulation duration of 60 s. This interval was chosen to ensure an accurate representation of dynamic system responses under varying operational conditions. The simulation environment and hardware specifications are Windows 10 (64-bit), Intel Core i7, 3.4 GHz, and RAM: 16 GB. These specifications provided a stable and efficient simulation environment, ensuring smooth operation and high computational accuracy. This setup allowed the study to achieve reliable and replicable results, supporting the research's objectives and validating the proposed methods.

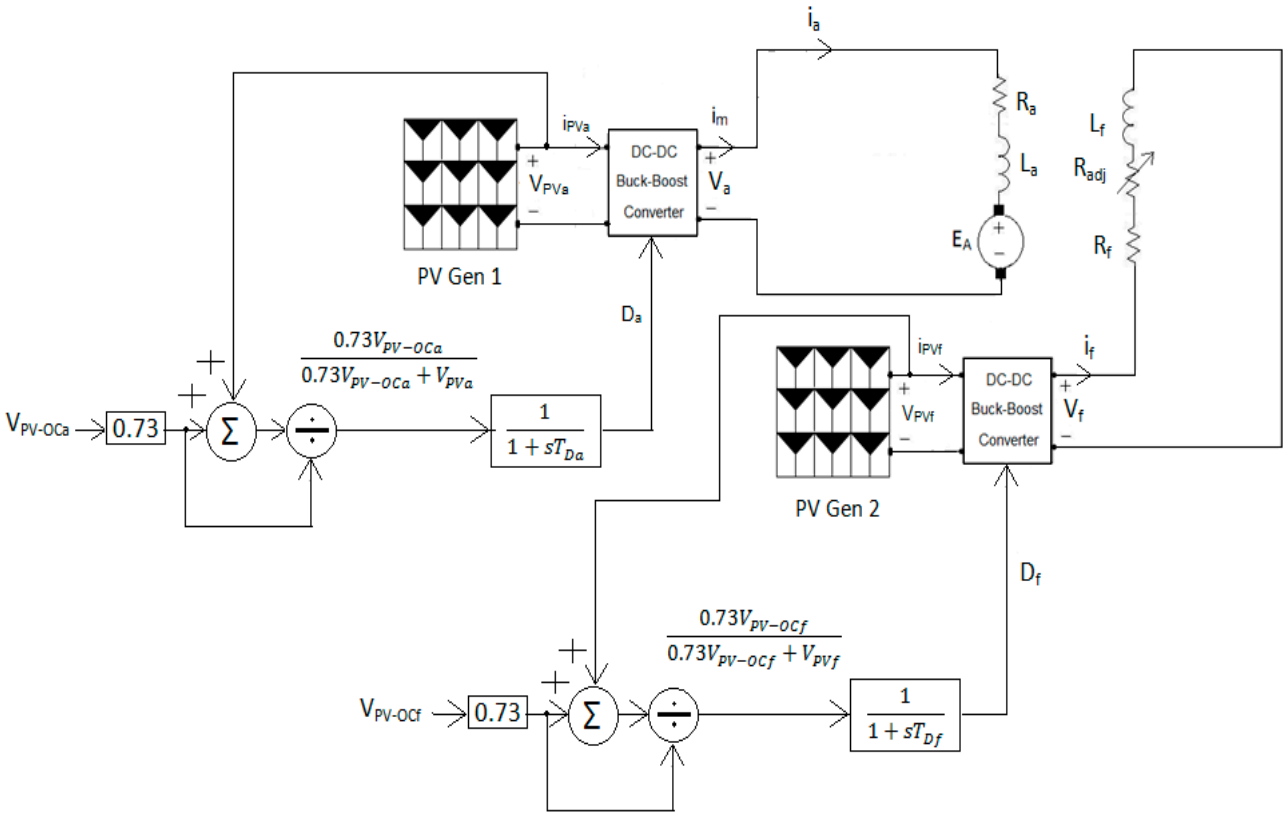

Figure 1. Schematic diagram of PV generators with an SEDC motor system.

2.2. Design of Photovoltaic Generators and Dynamic Modelling of the System

In this section, we examine the design considerations relevant to the PV system, specifically emphasizing its output characteristics. These parameters include the voltage of the PVs to the output current and the associated output power generated by the system, across different levels of solar irradiance. Additionally, we present a brief overview of the mathematical equations that govern the operation of key components, including the SEDC motor, the DC-DC converter (buck–boost), and the voltage controllers utilized for MPP tracking.

2.2.1. Photovoltaic Design and Output Characteristics and Fractional Open-Circuit Voltage Controllers

PV systems consist of numerous PV cells organized into modules and configured in series–parallel arrangements to create PV arrays. This configuration is essential for maximizing power output to satisfy particular voltage and current demands. Each PV cell functions through the photovoltaic effect, which converts solar energy into electrical energy. The design of PV arrays, including the selection of the appropriate number of series and parallel connections, has an influence on the system's output characteristics, including the MPP, voltage, and current. The behaviour of a PV array is highly nonlinear due to the varying irradiance and temperature conditions. These characteristics are commonly represented by the current/voltage curve and the power/voltage curve. Therefore, the output current of the PV array, I_{arr}, as described by Equation (1), depends on the voltage of the PV array, V_{arr}, number of PV cells in series and parallel, n_{series} and $n_{parallel}$, diode current, I_{diod}, and the photocurrent, I_{pc}.

$$\mathrm{I_{arr}} = \mathrm{n_{parallel}I_{pc}} - \mathrm{n_{parallel}I_{diod}}\left(\mathrm{e}^{\left(\frac{\mathrm{e}}{\mathrm{ibt}}\frac{\mathrm{V_{arr}}}{\mathrm{n_{series}}}\right)} - 1\right) \quad (1)$$

where e represents the electron charge, valued at 1.602×10^{-19} C, i is a parameter that quantifies the deviation of a diode's behaviour, b refers to Boltzmann's constant, 1.38×10^{-23},

and t is the ambient temperature in Kelvin (K). Figure 2 presents the 10th-order polynomial approximation representing the voltage as a function of the output current. These PV modules are utilized to supply power to both the armature and the field circuits of the SEDC motor, along with the corresponding output power. Additionally, Table 2 offers a comprehensive overview of the technical specifications of the PV generators utilized in the system.

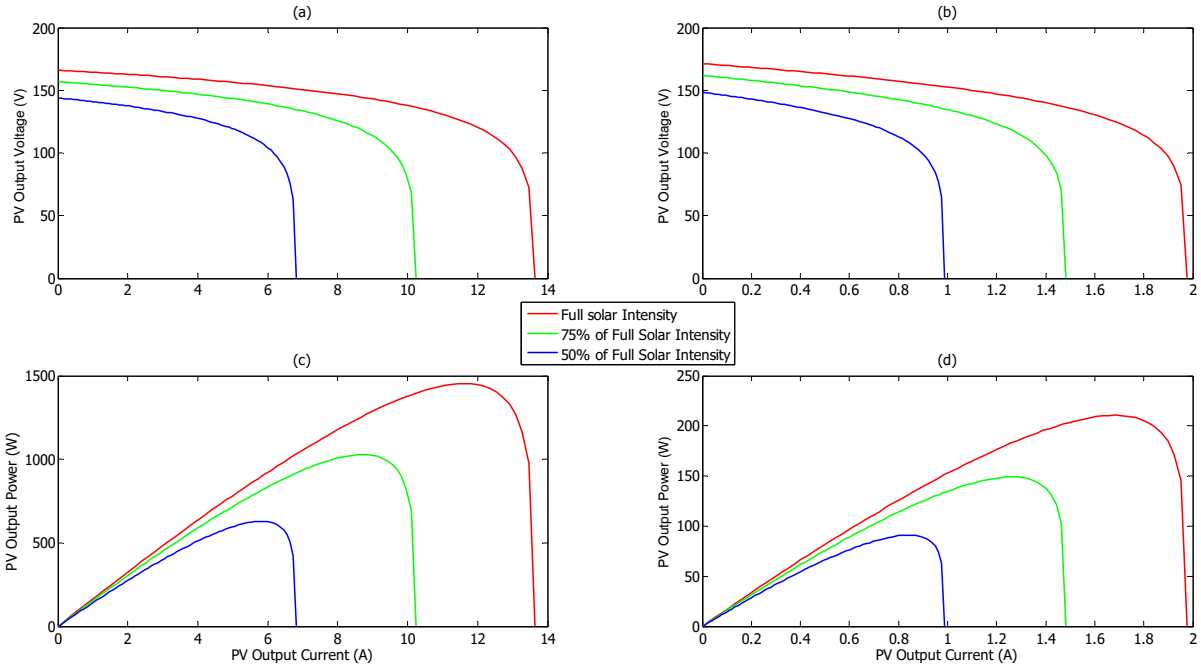

Figure 2. PV generators' characteristics for feeding armature and field circuits: (**a**) terminal output voltage as a function of PV current for the armature, (**b**) terminal output voltage as a function of PV current for the field, (**c**) corresponding output power for PV feeding armature, and (**d**) corresponding output power for PV feeding field.

Table 2. Specifications of the developed PV generators.

Parameter	Feeding Armature Circuit			Feeding Field Circuit		
	Intensity Level					
	100% (Full)	**75%**	**50%**	**100% (Full)**	**75%**	**50%**
Open-Circuit Voltage, V_{OC} (V)	166.2	157	143.9	171.4	161.9	148.5
Short-Circuit Current, I_{SC} (A)	13.65	10.24	6.824	1.978	1.484	0.989

As depicted in Figure 2, the relationship between the PV voltage and current exhibits notable nonlinearity. To accurately model this behaviour, a 10th-order polynomial function has been employed for approximation, utilizing MATLAB [14,15]. Detailed nomenclatures are provided in Appendix A, while the numerical values of the polynomial constants for Equations (2) and (3) can be referenced in Tables A1 and A2, respectively, in Appendix A. Furthermore, Appendix A lists the numerical parameters of the system. Equation (2) represents the 10th order polynomial, from h equal 1 to 11, of the characteristics of motor armature circuits with highly nonlinear behaviour. The output voltage of the armature circuit of the array, V_{array1}, based on the polynomials' constant, Q, is described as follows:

$$\mathrm{V_{array1}} = \sum_{\mathrm{h}=1}^{11} \mathrm{Q_h I_{array1}^{11-h}} = \mathrm{Q_1 I_{array1}^{10}} + \mathrm{Q_2 I_{array1}^{9}} + \ldots + \mathrm{Q_{11}} \quad (2)$$

This behaviour of the filed circuit is described by Equation (3). The output voltage of the field circuit of the array, V_{array2}, based on polynomials constant, β, is described as follows:

$$V_{array2} = \sum_{h=1}^{11} \beta_h I_{array2}^{11-h} = \beta_1 I_{array2}^{10} + \beta_2 I_{array2}^{9} + \ldots + \beta_{11} \quad (3)$$

Equation (4) describes the fractional open-circuit voltage that is needed in Equations (2) and (3). Mathematically, this relationship can be expressed as follows:

$$V_{MPP} = KV_{OC} \quad (4)$$

In this study, the fraction of the open-circuit voltage for the maximum power point operating voltage (V_{MPP})value, denoted as (k), is specified as 0.73. This selection falls within the typical range of 0.7 to 0.85. In this work, we enhance the proportional open-circuit voltage method to achieve a more stable and reliable MPPT under fluctuating irradiance conditions. Our method optimizes energy use by integrating two separate PV generators that power distinct motor circuits (armature and field). The incorporation of polynomial modelling improves the accuracy of voltage–current relationships, leading to better energy utilization. Unlike previous studies that rely on static MPPT techniques, our approach dynamically adjusts the duty cycle of the DC-DC converters in real time. This adaptive strategy ensures peak performance across different solar intensities, leading to improved efficiency and reliability in practical applications. The RTDS NovaCore 2.0, with its high processing power and flexibility, supports this dynamic adjustment process, enabling real-time simulation and precise control under varying conditions.

2.2.2. Mathematical Dynamic Model for SEDC Motors

In an SEDC motor, the two circuits (field and armature) operate independently and are supplied by separate sources. The nonlinear dynamical mathematical model of the SEDC motor is as follows [14,15]:

$$L_a \frac{di_a}{dt} = V_a - i_a R_a - K\Phi\omega \quad (5)$$

$$L_f \frac{di_f}{dt} = V_f - i_f R_f \quad (6)$$

$$J \frac{d\omega}{dt} = K\Phi i_f - T_l - B\omega \quad (7)$$

where L_a and L_f represent the inductance of the armature and field windings, respectively, R_a denotes the resistance of armature, R_f signifies the resistance of field winding, J indicates the moment of inertia for the rotor and load, and ω represents the rotor's rotational speed. V_a: Armature voltage; V_f: Field voltage; K: constant depends on the design of the machine. Φ: flux; and T_l: torque of load. The numerical values of the polynomial constants for Equation (8) that represent the magnetization curve can be found in Appendix A, specifically in Table A3 [15].

$$K\Phi = \sum_{n=1}^{6} \gamma_n i_f^{6-n} = \gamma_1 i_f^5 + \gamma_2 i_f^4 + \ldots + \gamma_6 \quad (8)$$

where γ is the constants of the polynomial that represents the magnetization curve. Equation (8) presents nonlinear polynomial curve fitting for the ferromagnetic material in the motor, which was generated using MATLAB software. It is well established that Maximum Power Point Tracking (MPPT) of a photovoltaic (PV) generator occurs at a fraction of the open-circuit voltage [15]. This method relies on a proportional relationship between the open-circuit voltage and the maximum power point (MPP) voltage. The integration of dual PV generators to independently power the armature and field circuits of a separately excited DC motor enables precise and dynamic tracking of the MPP. Additionally,

polynomial modelling improves the accuracy of voltage–current relationships, optimizing energy utilization. Thus, the proposed technique uniquely combines the fractional open-circuit voltage method with dual PV systems to enhance energy output. By dynamically adjusting the duty cycle of buck–boost converters, the method ensures both stability and efficiency under varying solar irradiance conditions, improving on traditional static MPPT approaches. Consequently, estimating the MPP involves measuring the open-circuit voltage and comparing it with the PV voltage.

2.2.3. DC-DC Converters (Buck–Boost)

DC-DC switched-mode converters are essential in PV systems, serving as an intermediary between the terminals of the PV generator. Their main function is to modify the operating voltage to either match the value at the MPP of the PV generator or a fraction of the open-circuit voltage. These converters typically consist of lossless components such as inductors and capacitors, along with power semiconductor switches [22–28]. The switches are usually managed using Pulse Width Modulation (PWM) techniques. In the proposed system, buck–boost circuits are employed, where the average output voltage is represented as a function of the voltages of PVs and the duty cycles of the switches, namely the armature duty cycle (D_a) and field duty cycle (D_f), given as follows:

$$V_a = \frac{D_a}{1 - D_a} V_{PVa} \tag{9}$$

$$V_f = \frac{D_f}{1 - D_f} V_{PVf} \tag{10}$$

The output current from the converters, assuming an ideal converter circuit, can be defined as a function of the currents. Equation (11) represents the motor armature current (i_a) of the buck–boost at the armature circuit based on the armature current fed from the PV generator (i_{PVa}), while Equation (12) describes the motor field current (i_f) based on the field current fed from its PV generator (i_{PVf}).

$$i_a = \frac{1 - D_a}{D_a} i_{PVa} \tag{11}$$

$$i_f = \frac{1 - D_f}{D_f} i_{PVf} \tag{12}$$

The voltage controllers for the armature and field circuits of the SEDC motor are shown in Figure 1. These controllers are designed to manage the voltage in their respective circuits by utilizing fractional open-circuit voltage values from the PV generator. This method ensures optimal performance under various motor loading conditions and different levels of solar irradiance, facilitating MPPT through the automatic adjustment of each DC-DC buck–boost converter's duty cycle. The behaviour of the voltage controllers for both the armature and field circuits can be represented as follows:

$$T_{D_a} \frac{dD_a}{dt} = \frac{0.73 V_{pv\_OCa}}{0.73 V_{OCa} + V_{PVa}} - D_a \tag{13}$$

$$T_{D_f} \frac{dD_f}{dt} = \frac{0.73 V_{PV\_OCf}}{0.73 V_{OCf} + V_{PVf}} - D_f \tag{14}$$

Substituting Equations (2) and (3) in Equations (13) and (14) become

$$T_{D_a} \frac{dD_a}{dt} = \frac{0.73 V_{PVOCa}}{0.73 V_{OCa} + \sum_{n=1}^{11} \alpha_n I_{PVa}^{11-n}} - D_a \tag{15}$$

$$T_{D_f} \frac{dD_f}{dt} = \frac{0.73 V_{PV\_OCf}}{0.73 V_{PV\_OCf} + \sum_{n=1}^{11} \beta_n I_{PVf}^{11-n}} - D_f \tag{16}$$

where T_{D_a} and T_{D_f} represent time constants of the duty cycles of converters interfaced to SEDC motor armature and field circuits, respectively.

3. Numerical Simulations and Analysis

In this section, the results from numerical simulations performed on the nonlinear dynamic model of the system are discussed. These simulations were conducted in response to changes in the mechanical load (T_l) applied to the SEDC motor, while taking into account both full and partial intensification of the PV generator. Furthermore, this research examines the motor's response to load changes at 100%, 75%, and 50% of full solar irradiance, alongside steady-state output characteristics under various solar intensities.

3.1. System Performance Under Full Solar Irradiance and Varied Motor Loading

In Figures 3 and 4, the system's response is shown under full intensity as the T_l with successive reductions from 10 N.m to 7 N.m and then to 4 N.m. The results demonstrate that as the load diminishes, the motor's speed increases, while the duty cycle of the DC-DC converter decreases accordingly. This behaviour highlights the system's capacity to adeptly adjust to varying load conditions. To maintain the maximum power of the PV, corresponding to the terminal voltage of 123 V for the motor, adjustments to the buck–boost converter's duty cycle in the armature circuit are implemented. The PV output terminal voltages supplying the armature circuit of the SEDC motor also vary with the load torque (T_l), showcasing the system's dynamic response to changing conditions. The armature current of the SEDC motor varies under different load conditions, reflecting the changes in torque and speed. Despite these variations, the terminal voltage of the motor remains constant, indicating effective control mechanisms in place to maintain stable operation. The system's response time under peak solar exposure is approximately 50 s, suggesting a reasonably fast response to changes in solar irradiance. Additionally, the behaviour of the buck–boost armature chopper as a step-down or step-up converter depending on the duty cycle highlights its versatility in optimizing power transfer efficiency. Overall, the findings demonstrate the system's capability to efficiently utilize solar energy for motor operation, showcasing its potential for sustainable and reliable performance in practical applications.

3.2. System Behaviour at 75% Solar Intensity and Varied Motor Loading

In Figures 5 and 6, we observe the system's response under 75% of full solar intensity, illustrating the impact of step changes in the T_l from 3 N.m to 5 N.m and then to 7 N.m. Initially, at 3 N.m, the motor operates at 1518 rpm with a duty cycle of 0.4381. As the T_l increases to 5 N.m, the motor's speed decreases to 1509 rpm, with a duty cycle of 0.4587. Further increasing the torque to 7 N.m results in a speed of 1500 rpm and a duty cycle of 0.5437. To sustain the MPP of the PVs at 75% of full intensity (115 V), adjustments are made to the duty cycle in the armature circuit. Specifically, the PV output terminal voltages supplying the armature circuit of the motor measure 147.5 V, 135.7 V, and 96.52 V after the load torque escalates from 3 N.m to 5 N.m, and then to 7 N.m, respectively. The simulations (Figures 5 and 6) illustrate that the armature current of the SEDC motor varies from 4.182 A to 6.969 A to 9.757 A under these varying load conditions. Meanwhile, the terminal output voltage of the PV generator supplying the field circuit is maintained at 137.17 V, with a converter duty cycle of 0.4628. Across all load conditions, the motor's terminal voltage stays steady, consistent with the fractional open-circuit voltage values of the PV generators at 75% of full solar irradiance levels supplying both the armature and field circuits. These values are in line with the preset values of the armature and field voltage controllers. The settling time of the system under 75% of full solar intensity is approximately 58 s, suggesting a reasonably swift response to fluctuations in solar irradiance. This behaviour highlights the system's flexibility and efficacy in connecting solar energy for motor operation.

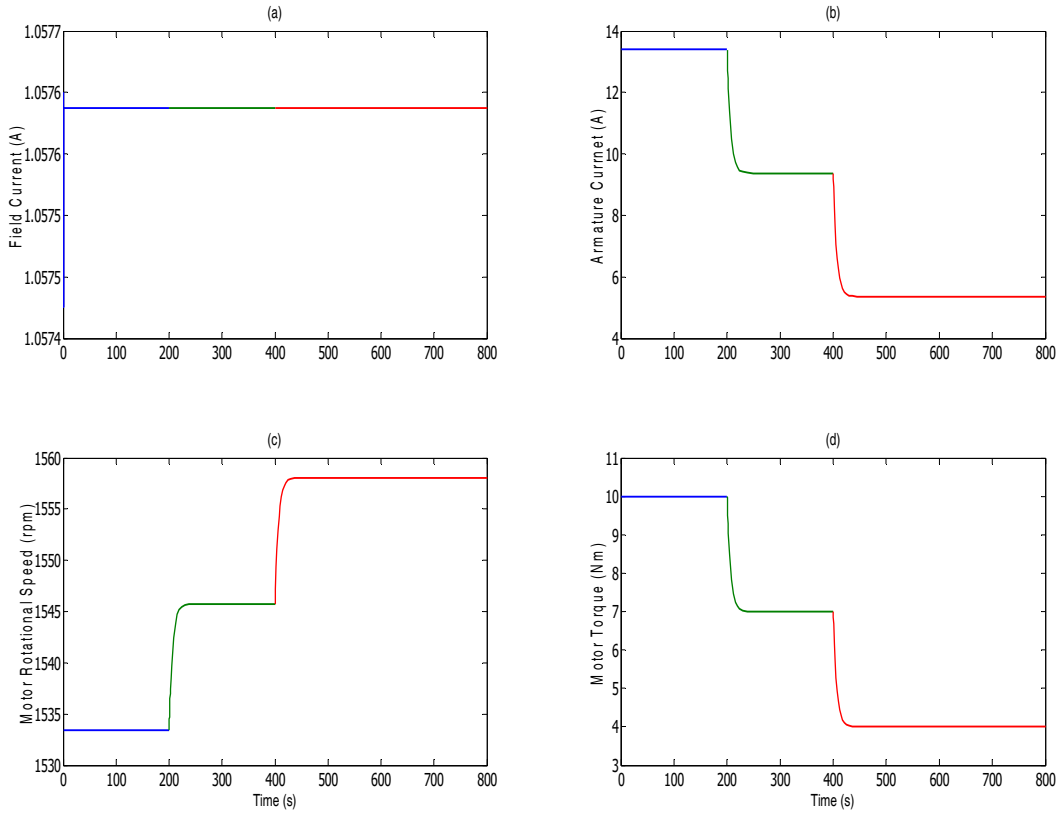

Figure 3. The response of the system under full solar irradiance to step changes in mechanical loads, showing motor current for (**a**) field, (**b**) armature, (**c**) rotational speed, and (**d**) motor torque.

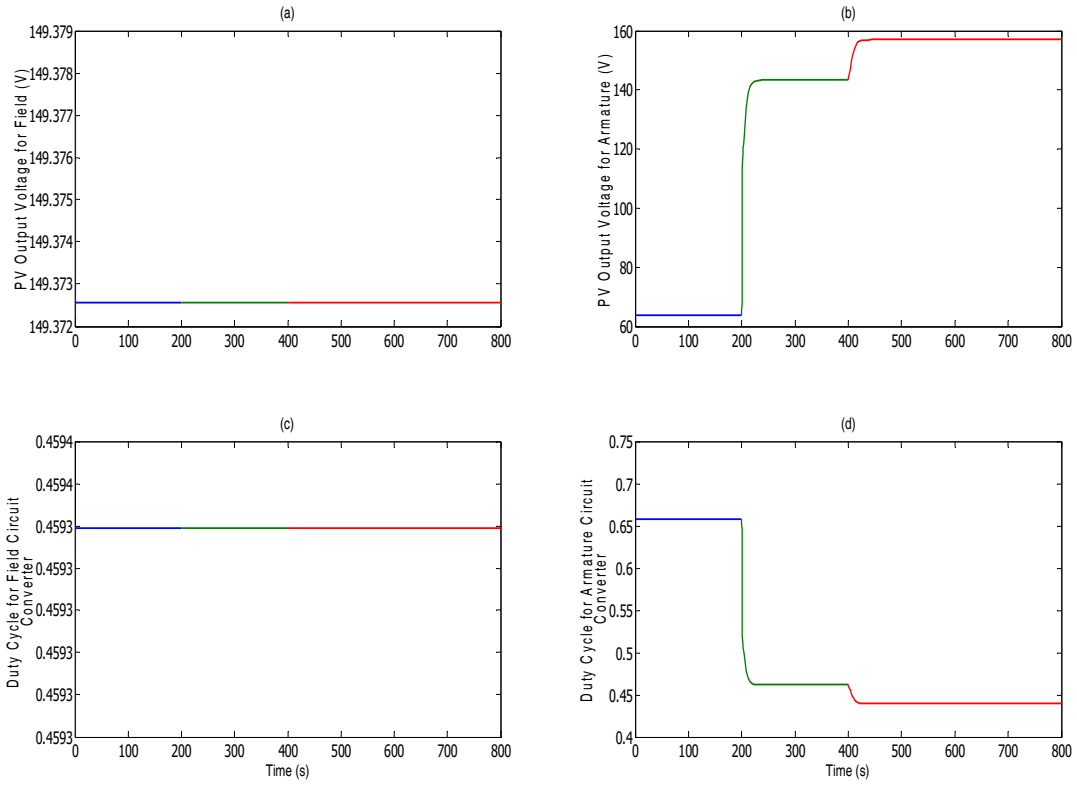

Figure 4. The PV output voltage feeds the (**a**) field circuit and (**b**) armature circuit, along with the duty cycle for the buck–boost converter for the (**c**) field circuit and (**d**) armature circuit, after step changes in loads under full irradiance.

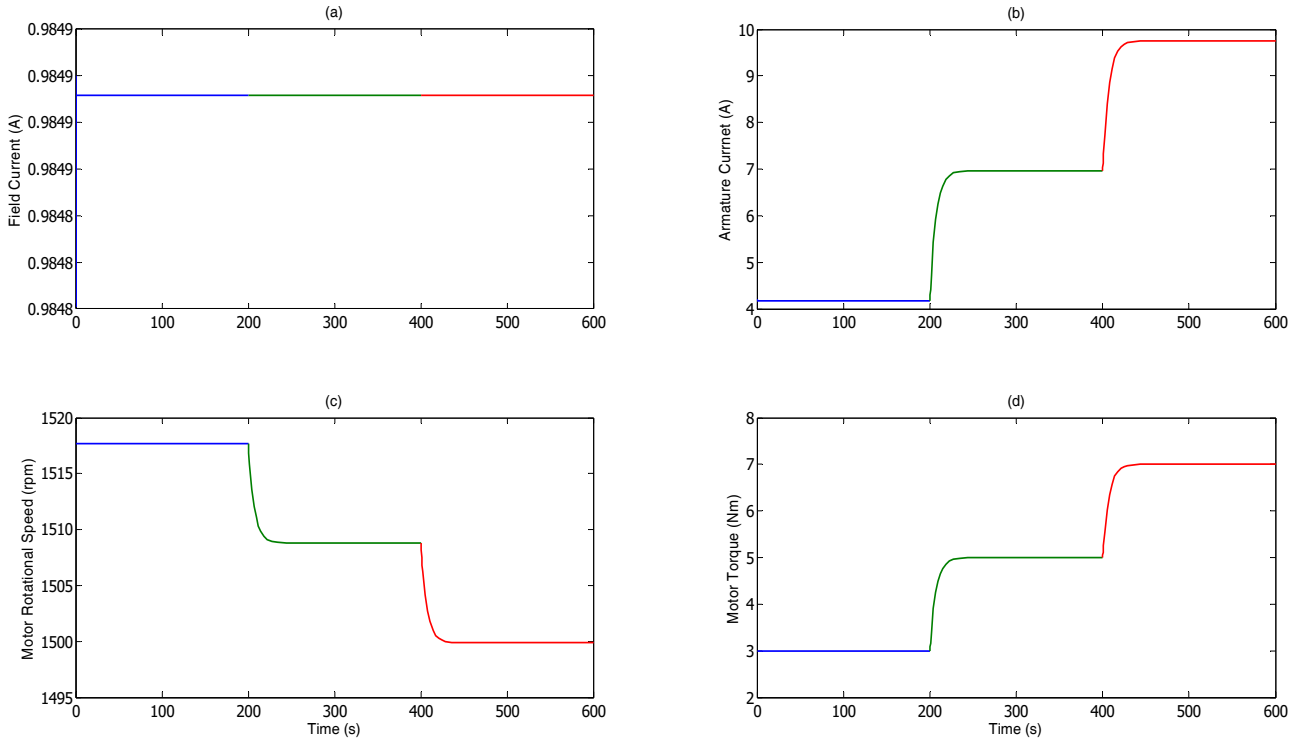

Figure 5. Motor, (**a**) field current, (**b**) armature current, (**c**) rotational speed, and (**d**) torque following step changes in mechanical loads at 75% of full solar irradiance.

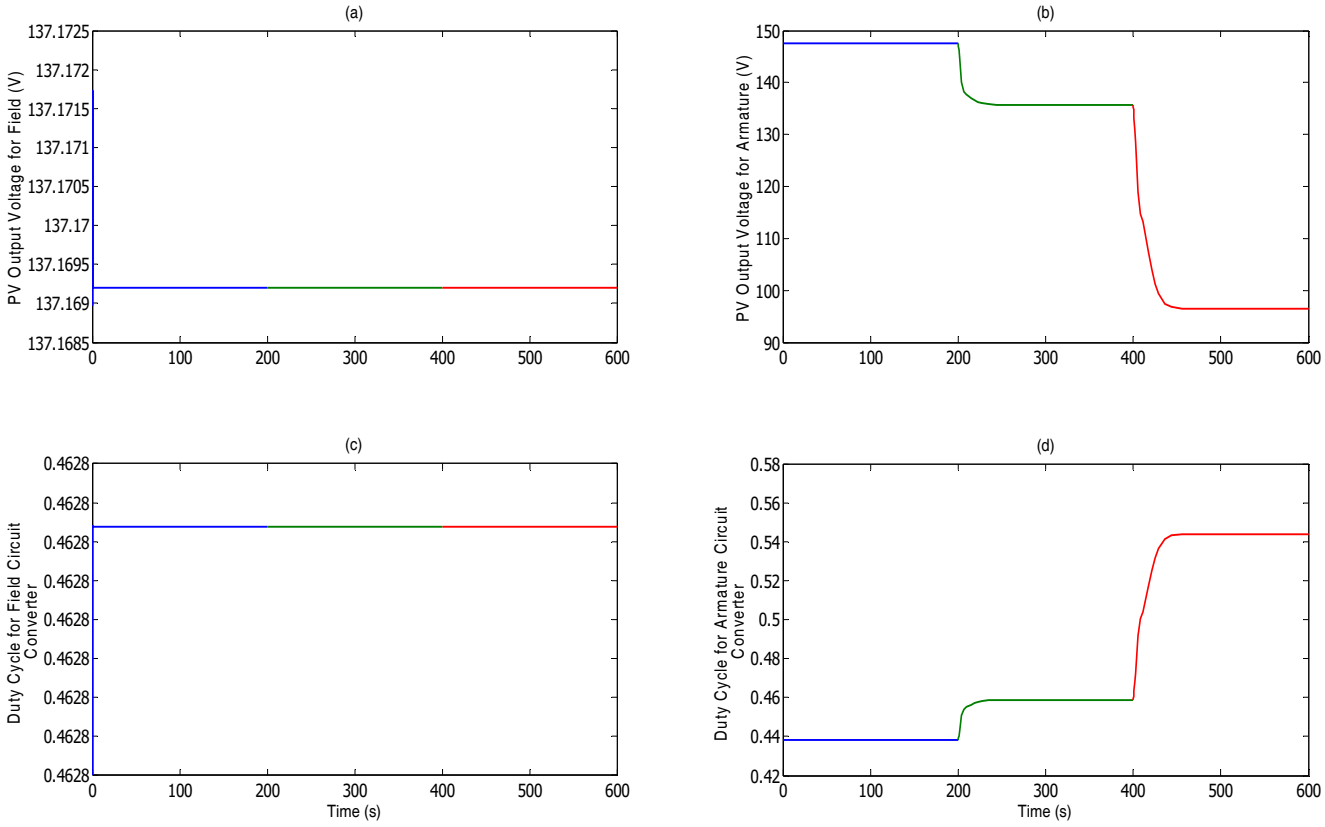

Figure 6. The PV output voltage feeding the (**a**) field circuit and (**b**) armature circuit, along with the duty cycle for the buck–boost converter for the (**c**) field circuit and (**d**) armature circuit, after step changes in mechanical loads at 75% of full solar irradiance.

3.3. System Behaviour at 50% Solar Intensity and Varied Motor Loading

Figures 7 and 8 show the system's response under 50% of full solar intensity, showcasing the effects of step changes in the T_l from 2 N.m to 0 N.m (No Load) and then to 4 N.m. In the first step, at 2 N.m, the motor operates at 1461 rpm with a duty cycle of 0.4388. Upon reducing the load to 0 N.m, the motor's steady-state speed increases to 1471 rpm, accompanied by a converter duty cycle of 0.4181. Subsequently, increasing the torque to 4 N.m yields a speed of 1451 rpm and a duty cycle of 0.4986. To maintain the MPP of the PVs at 50% of full intensity (105.5 V), adjustments are made to the buck–boost converter's duty cycle in the armature circuit. The PV output terminal voltages supplying the armature circuit of the motor measure 134.2 V, 146 V, and 105.5 V after the load torque decreases from 2 N.m to 0 N.m and then increases to 4 N.m, respectively. The simulations indicate that the armature current of the SEDC motor varies from 2.936 A to 0 A to 5.872 A under these fluctuating load conditions. Meanwhile, the terminal output voltage of the PV generator supplying the field circuit is maintained at 102.5 V, with a converter duty cycle of 0.514. Throughout all load conditions, the motor's terminal voltage remains constant, consistent with the fractional open-circuit voltage values of the PV generators at 50% of full solar irradiance levels supplying both the armature and field circuits. These values align with the predetermined values of the armature and field voltage controllers. The settling time of the system under 50% of full solar intensity is approximately 65 s, indicating a relatively swift response to changes in solar irradiance. This behaviour highlights the system's versatility and efficiency in utilizing solar energy for motor operation across various conditions.

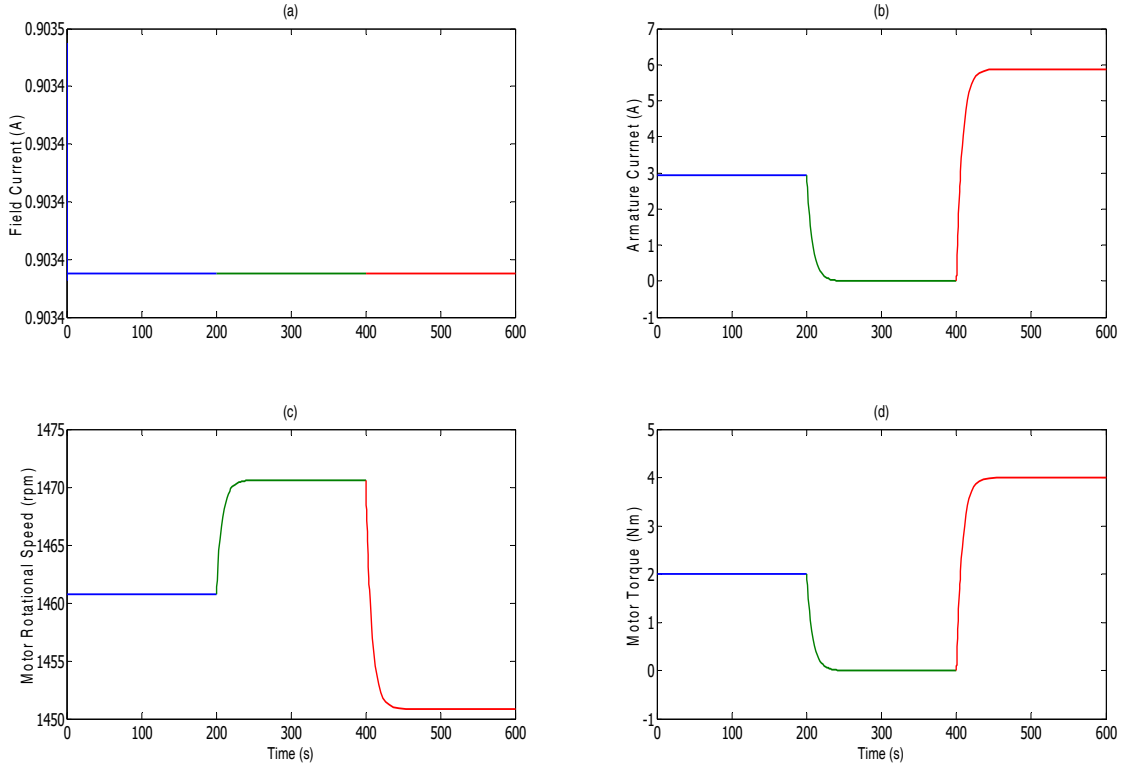

Figure 7. Motor, (**a**) field current, (**b**) armature current, (**c**) rotational speed, and (**d**) torque following step changes in mechanical loads at 50% of full solar irradiance.

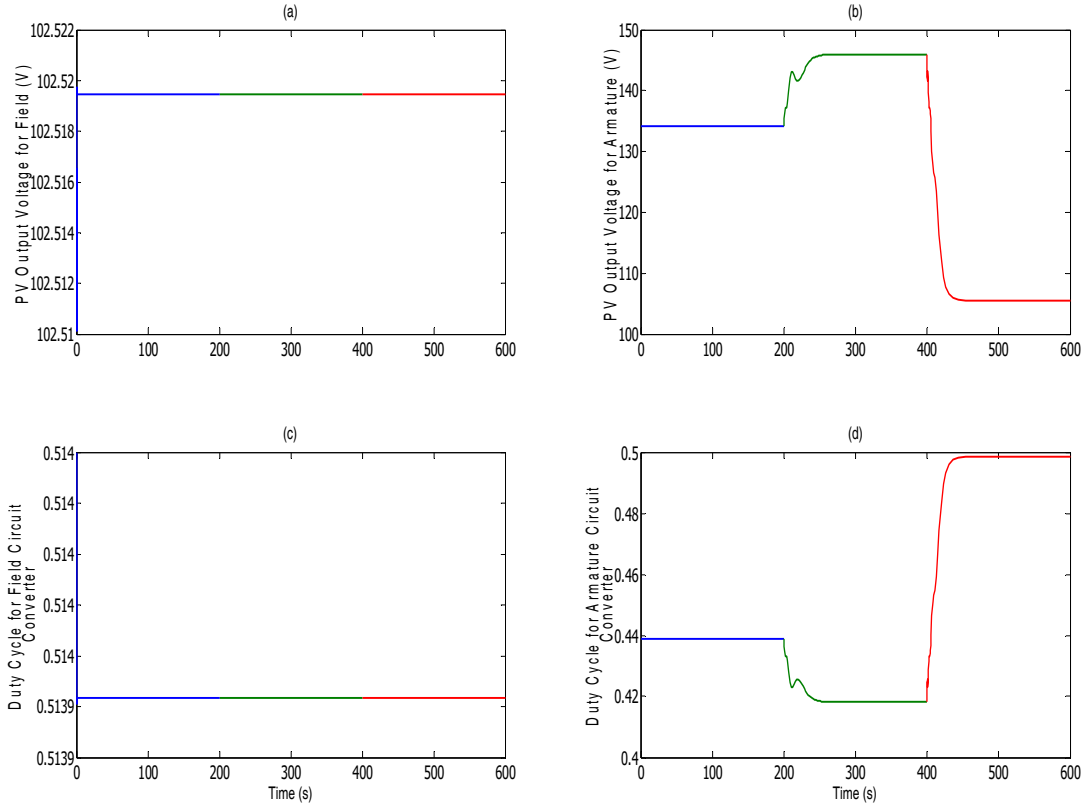

Figure 8. The PV output voltage feeding the (**a**) field circuit and (**b**) armature circuit, along with the duty cycle for the buck–boost converter for the (**c**) field circuit and (**d**) armature circuit, after step changes in mechanical loads at 50% of full solar irradiance.

3.4. Steady-State Output Characteristics of a DC Separately Excited Motor Under Various Solar Irradiance Levels

Table 3 illustrates that the steady-state parameters of the system exhibit variations across three levels of solar radiation and various motor load conditions. This research focuses on examining the output characteristics, particularly the torque–speed relationships of a DC separately excited motor powered and excited by photovoltaic generators under varying illumination levels. To identify the system's operating points, the dynamical differential equations describing the entire system are developed. Subsequently, the resulting nonlinear equations were solved using MATLAB software. Figure 9 illustrates the torque–speed characteristics of the DC separately excited motor under different solar irradiance levels. This shows that at the rated load torque, the rotational speed of the DC separately excited motor behaves consistently across all solar intensity levels. However, the characteristics at 75% and 50% of full illumination are lower than at 100% of the full solar irradiance level. This difference occurs because the voltage supplied by the PV generators is lower under reduced loads, whereas the terminal voltages of the PV generators are higher due to lower current drawn from the cells. Overall, the findings suggest that the performance of the DC separately excited motor varies with the solar irradiance level, with lower illumination levels resulting in reduced motor performance as compared to [29,30]. The proposed algorithm achieved MPPT efficiency consistently, exceeding 95% under varying solar intensities, demonstrating its ability to maximize energy extraction from the PV system. It maintained reliable performance, evidenced by stable motor speed and consistent torque output, even during fluctuations in solar irradiance. This operational stability ensures that the system remains functional and dependable across diverse lighting conditions, making it suitable for real-world applications where environmental variability is a factor. These results highlight the algorithm's effectiveness in optimizing system operation and enhancing overall energy utilization.

Table 3. Steady-state parameters of the system at three solar irradiance levels and different motor loading conditions.

Parameters	**100% of Solar Irradiance**			**75% of Full Solar Irradiance**			**50% of Full Solar Irradiance**		
The step change in motor load torque T_L (N.m)	10	7	4	3	5	7	2	0	4
Motor armature current I_A (A)	13.4	9.379	5.36	4.182	6.969	9.757	2.936	0	5.872
Motor field current I_F (A)	1.058	1.058	1.058	0.9849	0.9849	0.9849	0.9034	0.9034	0.9034
Motor rotational speed, n_M (rpm)	1533	1546	1558	1518	1509	1500	1461	1471	1451
Duty cycle of the DC-DC converter for the armature circuit, D_a	0.6581	0.4619	0.4394	0.4381	0.4587	0.5438	0.4388	0.4181	0.4986
V_{array} for armature circuit (V)	63.94	143.4	157	147.5	135.7	96.52	134.2	146	105.5
Motor armature voltage at MPP (V)		123.07			115			105.4	
The duty cycle for the filed circuit, D_f	0.4593	0.4593	0.4593	0.4628	0.4628	0.4628	0.514	0.514	0.514
V_{array} for field circuit (V)	149.4	149.4	149.4	137.2	137.2	137.2	102.5	102.5	102.5
Motor field terminal voltage at MPP (V)		127			118.2			108.4	

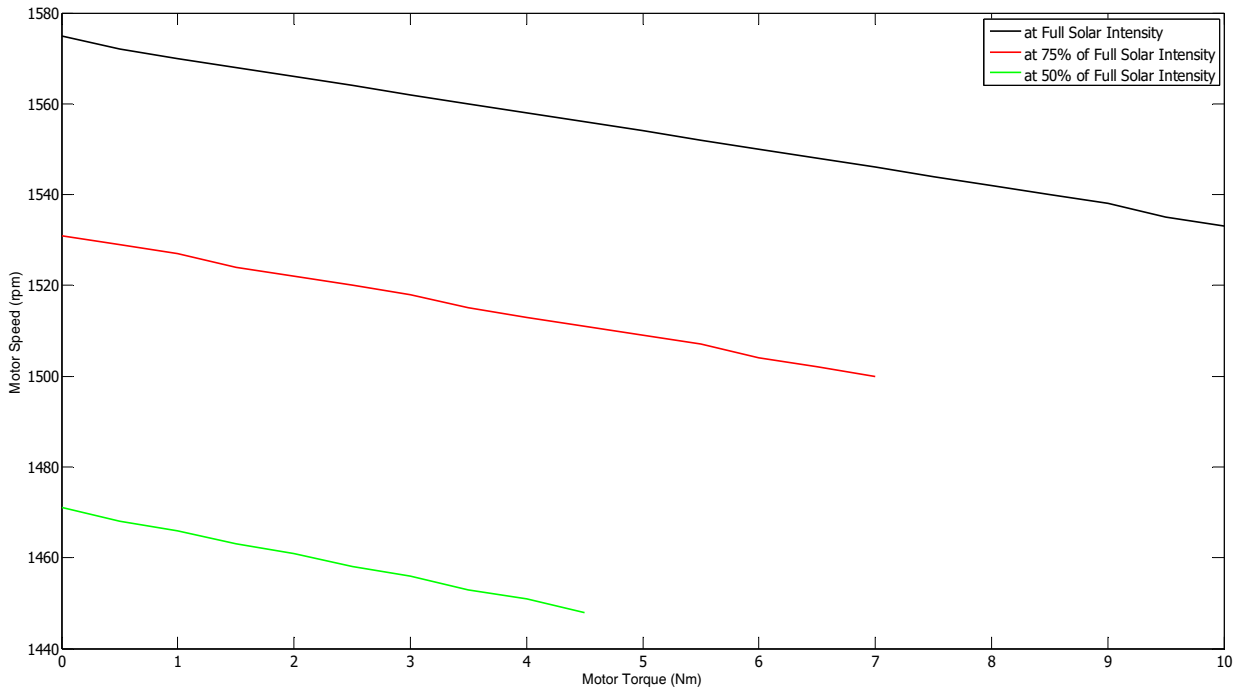

Figure 9. Torque–speed characteristics of a DC separately excited motor change when powered by photovoltaic (PV) generators under different illumination levels.

Table 3 shows how the motor system adapts to varying solar irradiance and load conditions. As irradiance drops from 100% to 50%, motor torque decreases from 10 N.m to 4 N.m, and armature current reduces from 13.4 A to 5.36 A. Motor speed remains relatively stable, decreasing slightly from 1533 rpm to 1451 rpm. The duty cycle for the armature circuit adjusts accordingly, dropping from 0.6581 to 0.4181. Voltages across both armature and field circuits decrease with reduced irradiance, ensuring that the system operates near the maximum power point. These dynamic adjustments optimize energy utilization and maintain motor efficiency, demonstrating the system's adaptability for applications like remote power supplies and sustainable energy solutions.

3.5. Steady-State Output Characteristics Using a Realistic Model

The parameters of the system showed variations at three distinct solar radiation levels and under different load conditions, as discussed in Section 3.4. This research focuses on analyzing the steady-state output characteristics by developing a realistic model and utilizing the RTDS and high-performance computers. In this study, the RTDS NovaCore 2.0 was utilized as the primary processing unit for real-time digital simulation. NovaCore 2.0, the latest generation of RTDS central processing hardware, offers advanced flexibility, allowing it to function as a standalone unit or within a NovaCor cubicle integrated with additional RTDS processing and I/O hardware. This configuration significantly enhances simulation precision and efficiency. The platform enables the real-time analysis of both transient and steady-state behaviours in complex systems, providing a robust tool for validating system performance under practical operating conditions. This tool enables the simulation of the DC separately excited motor powered by photovoltaic generators, allowing for the real-time monitoring of system behaviour, as shown in Figure 10.

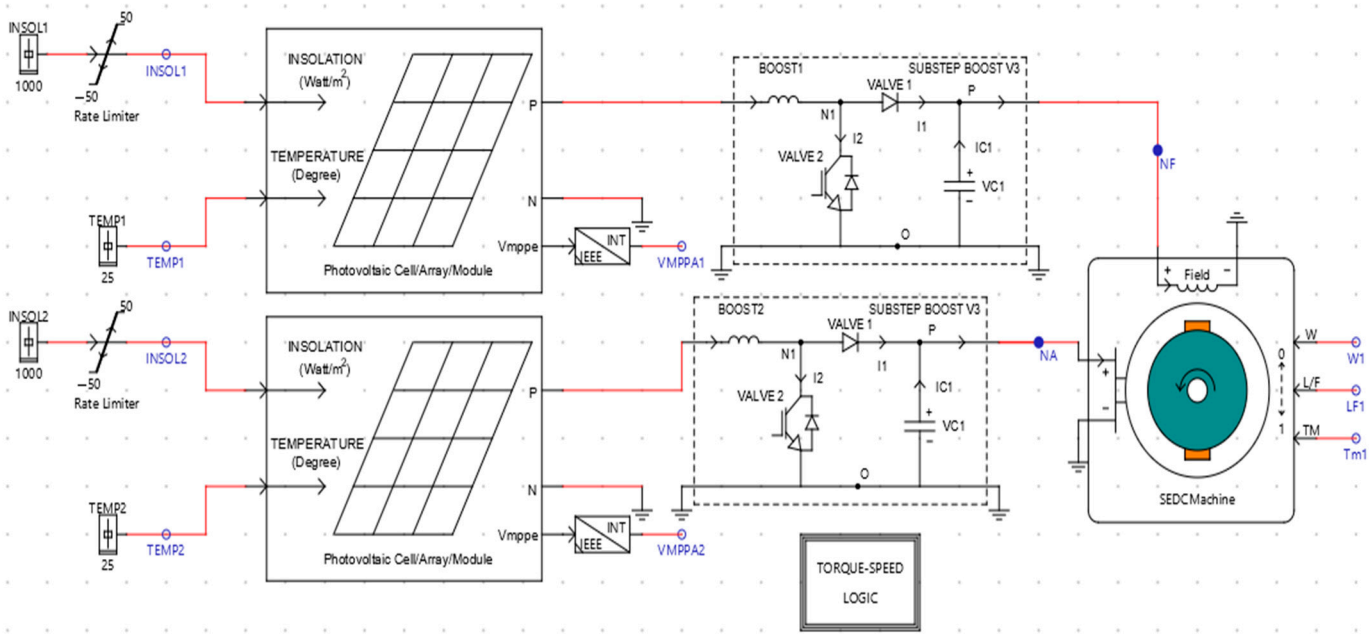

Figure 10. DC separately excited motor powered by photovoltaic (PV) generators using a real-time simulator, RTDS.

This study utilizes integration with RTDS to create realistic testing environments encompassing the power domain. The RTDS simulation demonstrates the system's capability to maintain stability despite fluctuations in solar irradiance levels, which influence the power supplied to the motor. As irradiance decreases, the motor adjusts its operating points to ensure consistent performance. At higher irradiance levels (100%, 75% and 50%), the armature current remains relatively constant, while it experiences a slight increase at 50% to generate sufficient torque despite the reduced input power. Additionally, the field current shows a minor decrease as irradiance diminishes, indicating that the motor's field control system is reducing field excitation to optimize power utilization. The observed decline in both armature and field voltages with decreasing irradiance is anticipated, as lower solar input leads to lower system voltages. The motor's rotational speed remains relatively stable across all irradiance levels, with only slight reductions (from 1038.6 RPM to 1031.1 RPM). This stability suggests that the system can maintain a consistent speed under varying power conditions, which is crucial for applications that require constant speed operation.

The following figures provide an in-depth analysis of the dynamic behaviour of a separately excited DC motor under different solar irradiance levels (100%, 75%, and 50%),

utilizing a Real-Time Digital Simulator (RTDS). This system creates a real-time simulation environment that effectively replicates the actual behaviour of electrical systems during dynamic transient operating conditions. In these RTDS validation analyses, the system operates with a torque of 5 N.m, and the motor parameters, including armature current, field current, armature voltage, field voltage, and rotational speed, are recorded at each irradiance level. Figure 11 illustrates the armature current of 6.8 A by the armature circuit when the load torque is suddenly adjusted to 5 N.m at 100% irradiance level. The field current of 1.1 A by the field circuit at the same condition, as shown in Figure 12.

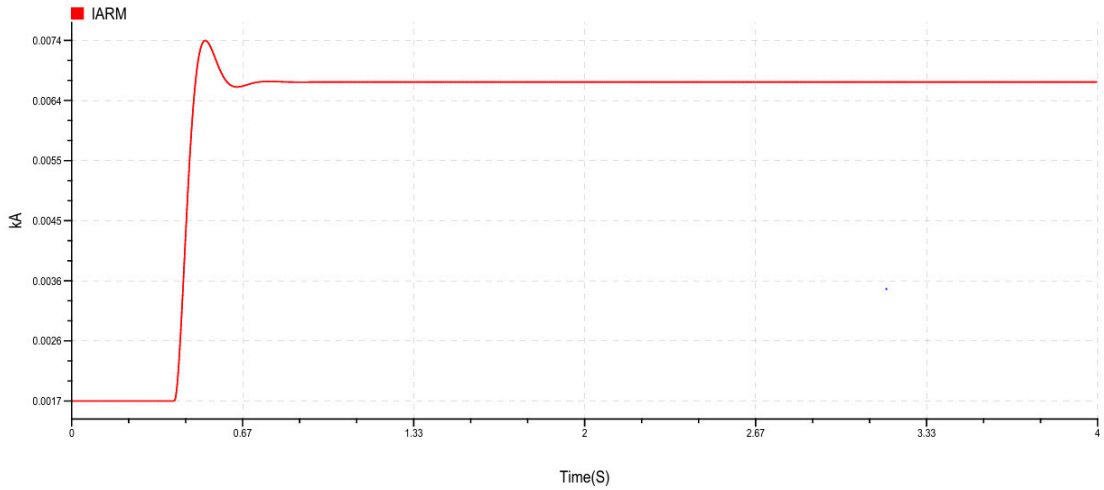

Figure 11. Armature current with 100% irradiance level.

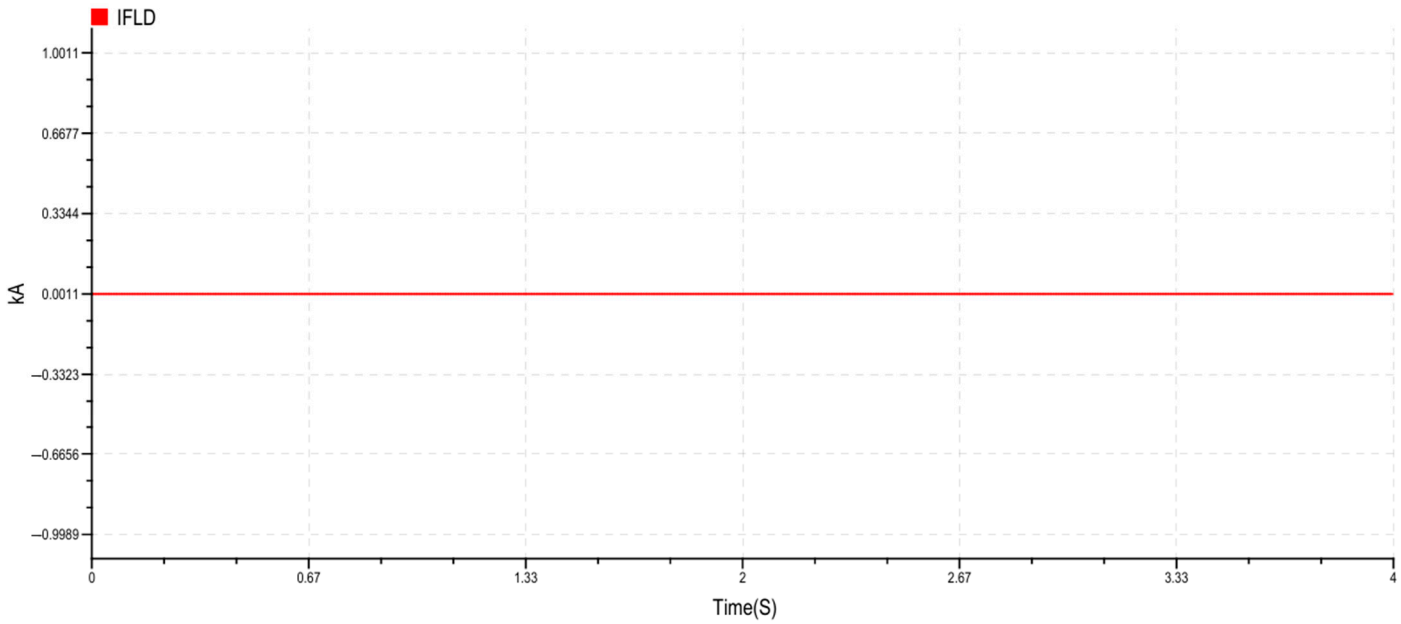

Figure 12. Field current with 100% irradiance level.

The armature voltage recorded at 149.8 V illustrates the electrical characteristics of the system when the load torque is suddenly adjusted to 5 N.m, as shown in Figure 13. This stable voltage output from the photovoltaic (PV) system reflects the ability of the solar energy source to provide consistent power under optimal irradiance conditions. The relatively high armature voltage indicates that the system can effectively drive the motor while maintaining adequate performance levels. The armature voltage is critical for ensuring the motor operates efficiently, as it directly influences the motor's torque

production and overall functionality. In parallel, the field voltage measured at 128.5 V supplied by the field PV system is crucial for energizing the field circuit of the motor, as shown in Figure 14. This voltage is essential for creating the magnetic field required for the motor's operation. The field voltage remains stable at this irradiance level, suggesting that the PV system can effectively supply the necessary excitation under varying load conditions. The field voltage's consistency contributes to the motor's ability to maintain its performance even with changes in load torque. Figure 15 motor rotational speed of (0.7 p.u) 1038.6 RPM as the load torque is step changed to 5 N.m. Table 4 shows how the system's steady-state parameters vary across three levels of solar irradiance and step change in motor load torque 5 N.m. This study focuses on analyzing the steady-state output characteristics, particularly the torque-speed relationship, of a DC separately excited motor that is powered and energized by photovoltaic generators under different illumination intensities using RTDS. Table 4 results show the motor's steady state operation under varying solar irradiance with a constant load torque of 5 N.m using RTDS. As irradiance decreases from 100% to 50%, armature current slightly increases from 6.8 A to 7.1 A, while field current remains stable at 1 A. Motor speed decreases only slightly from 1038.6 rpm to 1031.1 rpm. Both armature and field voltages decrease gradually, from 149.8 V to 141 V and from 128.5 V to 121.6 V, respectively. Overall, the system adjusts efficiently to changing conditions, maintaining stable performance despite reduced solar power.

Table 4. Steady-state parameters of the system at three solar irradiance levels and different motor loading conditions.

Parameters	100% of Solar Irradiance	75% of Full Solar Irradiance	50% of Full Solar Irradiance
The step change in motor load torque, N.m	5	5	5
Motor armature current, A	6.8	6.8	7.1
Motor field current, A	1.1	1	1
Motor rotational speed, (rpm)	1038.6	1035.9	1031.1
Armature voltage, V	149.8	146.4	141
Field voltage, V	128.5	125.8	121.6

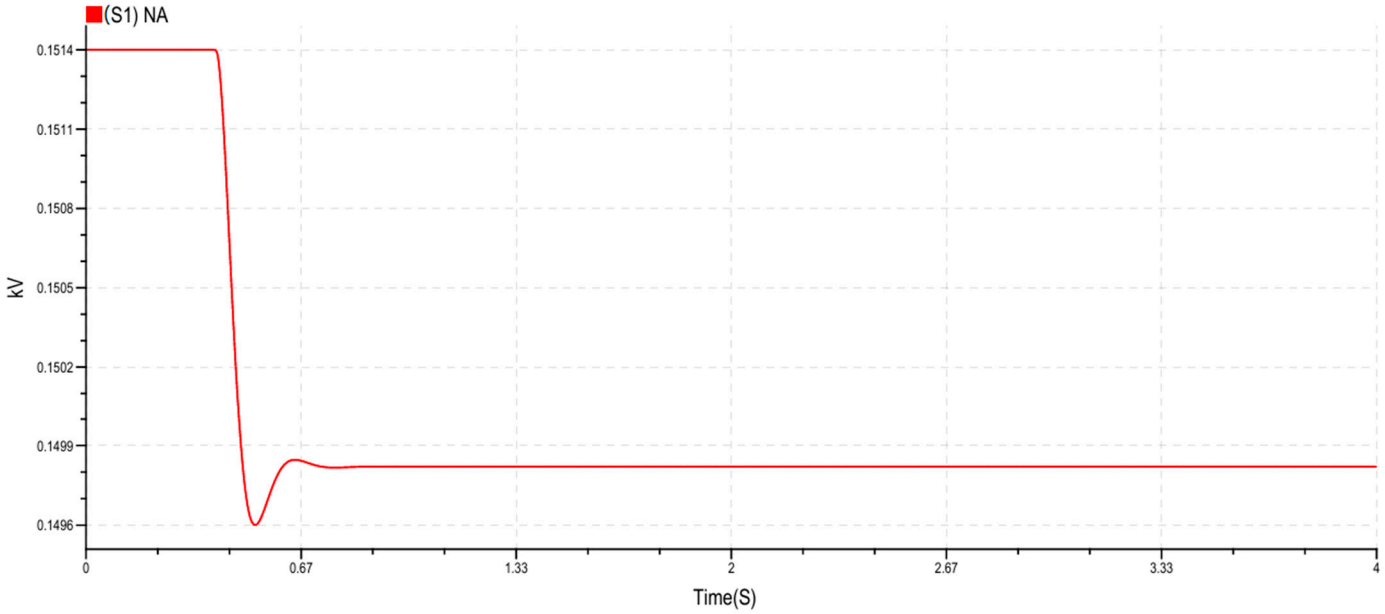

Figure 13. Armature voltage with 100% irradiance level.

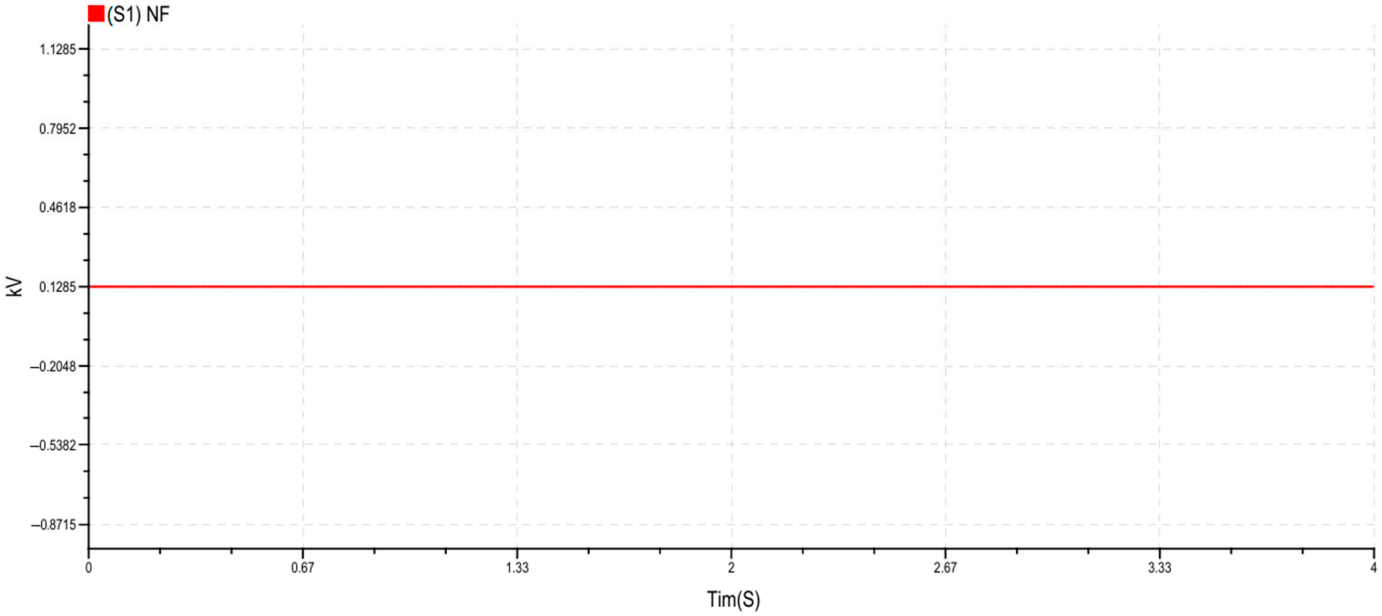

Figure 14. Field voltage with 100% irradiance level.

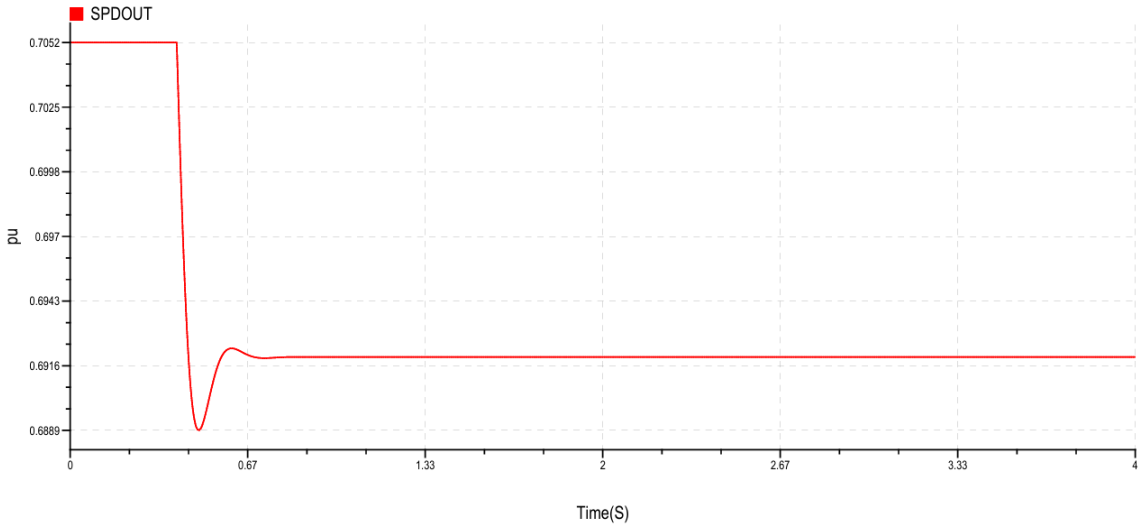

Figure 15. Motor rotational speed with 100% irradiance level.

The use of fractional open-circuit voltage (FOCV) ensured MPPT efficiency above 95%, aligning with studies [31] that validate the reliability and simplicity of this method in real-world applications. Furthermore, the system maintained stability under varying torque loads and solar irradiance, consistent with findings by [31], emphasizing the role of adaptive controls and converters in ensuring operational robustness. Steady-state performance showed that decreased solar irradiance was compensated by increased armature current, corroborating observations in [32] regarding the critical role of armature adjustments. The buck–boost converter's high efficiency in managing variable solar input aligns with the findings of [33], which highlight the converter's importance in maintaining system efficiency. Finally, the observed inverse relationship between torque and speed under low irradiance conditions mirrors trends reported by [34], emphasizing the need for advanced controls to mitigate performance loss. These findings validate the novel integration of dual PV systems with separately excited DC motors, addressing critical gaps in adaptive and efficient energy utilization.

4. Conclusions and Future Works

This study presents a detailed evaluation of the integration of PV generators in an SEDC motor, including MPPT techniques to optimize energy extraction. The proposed system demonstrated stable and consistent performance across varying solar irradiance levels (100%, 75%, and 50%) and mechanical load conditions. This performance was supported by the efficient use of buck–boost converters to regulate voltage and ensure optimal energy delivery. Under full irradiance, the motor operated at a rotational speed of approximately 1038 rpm with armature and field voltages of 150 V and 129 V, respectively, and a torque of 5 N.m. At 75% irradiance, the system adapted to slightly reduced conditions, achieving a speed of 1036 rpm and voltages of 146 V and 126 V. Even under 50% irradiance, the motor maintained a speed of 1031 rpm, with armature and field voltages of 141 V and 122 V, respectively. These results underline the system's resilience and ability to sustain performance, even with reduced solar energy input. The MPPT technique, using a fractional open-circuit voltage method with a fraction set at 0.73, adjusted the duty cycle of the buck–boost converter dynamically, ensuring efficient energy utilization. The system showed fast settling times between 50 and 65 s in response to changes in load and irradiance, demonstrating its adaptability to dynamic conditions. The duty cycle of the armature circuit adjusted between 0.44 and 0.66 approximately, depending on load and irradiance conditions. The system's performance was validated through real-time digital simulations, proving its ability to maintain stability and efficiency under transient conditions. While this study demonstrates the potential of the system for practical applications such as irrigation, ventilation, and standalone renewable energy systems, some limitations should be addressed in future research.

Future Works

In general, this study did not incorporate real-time weather data variability, which is crucial for optimizing system performance in actual operating environments. Variations in temperature, humidity, and cloud cover can significantly affect the system's efficiency, and real-time weather data should be included to improve model accuracy. Furthermore, this study assumed constant efficiencies for power converters and other components, but in real-world scenarios, their efficiencies can vary with operating conditions such as temperature and load. Future work should account for these variations to enhance the accuracy of performance predictions. Future directions could also involve exploring the integration of hybrid renewable energy sources, such as wind and battery storage systems, to further enhance system reliability and flexibility. The implementation of advanced intelligent control strategies could improve the system's performance, while scalability to industrial applications should be investigated to broaden its practical use. Additionally, assessing cost–benefit analyses, thermal management techniques, and the potential for grid integration would be crucial for improving the system's economic feasibility and operational efficiency. This work contributes to the advancement of sustainable energy solutions and sets the stage for further developments in renewable energy integration.

Author Contributions: Conceptualization, F.A. and M.I.A.; methodology, M.I.A., F.A., W.H. and T.O.S.; software, M.I.A., F.A. and T.O.S.; validation, F.A., T.O.S. and W.H.; formal analysis, M.I.A., F.A. and T.O.S.; investigation, All authors; resources, F.A. and M.I.A.; data curation, M.I.A. and T.O.S.; writing—M.I.A. and T.O.S.; writing—review and editing, All authors; visualization, All authors; supervision, F.A. and W.H.; project administration, F.A.; funding acquisition, F.A. All authors have read and agreed to the published version of the manuscript.

Funding: This work is supported by funding from the Scientific Research and Innovation Support Fund, Ministry of Higher Education Scientific Research, the Hashemite Kingdom of Jordan, under grant number (ENE/1/02/2022).

Data Availability Statement: Derived data supporting the findings of this study are available from the corresponding author on request.

Conflicts of Interest: The authors declare no conflicts of interest.

Nomenclature

Abbreviation	Description
PV	Photovoltaic.
SEDC	Separately Excited Direct-Current.
FLC	Fuzzy logic controller.
NN	Neural network.
PI	Proportional–Integral.
OID	Proportional–integral–derivative.
P&O	Perturbation and Observation.
PEMFC	Proton-Exchange Membrane Fuel Cells.
ASV-CSA	Adaptive Step Value with Cuckoo Search Algorithm.
PV-WPSs	Photovoltaic Water-Pumping Systems.
PSO	Particle Swarm Optimization.
RTDS	Real-time digital simulator.
MPPT	Maximum Power Point Tracking.
FOCV	Fractional open-circuit voltage.
DCSE	Direct current separately excited motor.
VPV	PV output terminal voltage.
I_{PV}	PV output current.
V_d	Output voltage of DC-DC buck–boost converter.
V_a	Armature terminal voltage of the SEDC motor.
V_f	Field terminal voltage of the SEDC motor.
I_{ph}	Photon current.
L_a	Armature winding inductance.
R_a	Armature winding resistance.
R_f	Field winding resistance.
L_f	Field winding inductance.
I_f	Motor field current.
I_a	Motor armature current.
I_m	Motor load current.
J	Rotor and load moment of inertia.
ω	Rotational speed of the rotor.
T_{Da}, T_{Df}	Time constants of the duty cycles of the DC-DC converters for armature and field circuits.
D_a	Duty cycle of the armature buck–boost circuit.
D_f	Duty cycle of the field buck–boost circuit.
K	Constant depending on the machine design.
Φ	Flux per pole.
T_L	Load torque.
I_{PV}	Output load current of the PV array (A).
V_{PV}	Output voltage of the PV array (V).
N_s	Number of series-connected PV cells.
N_p	Number of parallel-connected PV cells.
I_0	Reverse saturation current of the diode (A).
q	Elementary charge (~1.6×10^{-19} C).
n	Diode ideality factor.
k	Boltzmann's constant (~1.38×10^{-23} J/K).
T	Ambient temperature (K).
d/dt	Time derivative.

Appendix A

- The numerical values for the system's parameters are as follows: L_f = 10 mH, R_f = 120 Ω, V = 120 V, L_A = 18 mH, R_A = 0.24 Ω, J = 15 kg·m^2, T_{Da} = 1 ms, and T_{Df} = 0.1 ms.

Table A1. The constants for the output characteristics of the PVs, which power the armature circuit of the SEDC motor, are provided for three different solar irradiance levels.

	Full Solar Irradiance	**75% of Full Irradiance**	**50% of Full Irradiance**
Q_1 (V/A$^{10)}$	−0.0000002448	−0.00000409564	−0.00021566167
Q_2 (V/A^9)	0.000020221518	0.00025368261	0.0089053426
Q_3 (V/A^8)	−0.00071025735	−0.0066827305	−0.15639491
Q_4 (V/A^7)	0.013832714	0.097612823	1.5229452
Q_5 (V/A^6)	−0.16327544	−0.86413501	−8.9880971
Q_6(V/A^5)	1.1990814	4.7596023	33.003923
Q_7 (V/A^4)	−5.4118479	−16.111235	74.478767−
Q_8 (V/A^3)	14.277315	31.878	98.243414
Q_9 (V/A^2)	−19.834429	−33.214329	−68.241193
Q_{10} (V/A)	10.88503	13.670886	18.725203
Q_{11} (V)	147.89258	139.30756	127.20767

Table A2. The constants for the output characteristics of the PVs, which power the field circuit of the SEDC motor, are provided for three different solar irradiance levels.

	Full Solar Irradiance	**75% of Full Irradiance**	**50% of Full Irradiance**
β_1 (V/A$^{10)}$	−0.0000002448	−0.00000409564	−0.00021566167
β_2 (V/A^9)	0.000020221518	0.00025368261	0.0089053426
β_3 (V/A^8)	−0.00071025735	−0.0066827305	−0.15639491
β_4 (V/A^7)	0.013832714	0.097612823	1.5229452
β_5 (V/A^6)	−0.16327544	−0.86413501	−8.9880971
β_6 (V/A^5)	1.1990814	4.7596023	33.003923
β_7 (V/A^4)	−5.4118479	−16.111235	74.478767−
β_8 (V/A^3)	14.277315	31.878	98.243414
β_9 (V/A^2)	−19.834429	−33.214329	−68.241193
β_{10} (V/A)	10.88503	13.670886	18.725203
β_{11} (V)	147.89258	139.30756	127.20767

Table A3. The constants for the magnetization curve for the SEDC motor.

	Value
γ_1 (wb/A^5)	$-4.1835132 \times 10^{-20}$
γ_2 (wb/A^4)	$8.7567746 \times 10^{-19}$
γ_3 (wb/A^3)	5.494725×10^{-18}
γ_4 (wb/A^2)	−0.0037
γ_5 (wb/A^2)	0.138
γ_6 (wb/A^2)	0.0062

References

1. Frikha, M.A.; Croonen, J.; Deepak, K.; Benômar, Y.; El Baghdadi, M.; Hegazy, O. Multiphase Motors and Drive Systems for Electric Vehicle Powertrains: State of the Art Analysis and Future Trends. *Energies* **2023**, *16*, 768. [CrossRef]

2. Rafin, S.M.S.H.; Ahmed, R.; Haque, M.A.; Hossain, M.K.; Haque, M.A.; Mohammed, O.A. Power Electronics Revolutionized: A Comprehensive Analysis of Emerging Wide and Ultrawide Bandgap Devices. *Micromachines* **2023**, *14*, 2045. [CrossRef] [PubMed]
3. Wang, Z.; Li, J.; Hu, C.; Li, X.; Zhu, Y. Hybrid energy storage system and management strategy for motor drive with high torque overload. *J. Energy Storage* **2024**, *75*, 109432. [CrossRef]
4. Katche, M.L.; Makokha, A.B.; Zachary, S.O.; Adaramola, M.S. A Comprehensive Review of Maximum Power Point Tracking (MPPT) Techniques Used in Solar PV Systems. *Energies* **2023**, *16*, 2206. [CrossRef]
5. Kandemir, E.; Cetin, N.S.; Borekci, S. A comprehensive overview of maximum power extraction methods for PV systems. *Renew. Sustain. Energy Rev.* **2017**, *78*, 93–112. [CrossRef]
6. Guanghua, L.; Siddiqui, F.A.; Aman, M.M.; Shah, S.H.H.; Ali, A.; Soomar, A.M.; Shaikh, S. Improved maximum power point tracking algorithms by using numerical analysis techniques for photovoltaic systems. *Results Eng.* **2024**, *21*, 101740. [CrossRef]
7. Abuashour, M.I.; Sweidan, T.O. A Dynamical and steady state performance analysis of DC series motor and induction motor powered by an autonomous PV generator using MPPT. *Int. J. Eng. Syst. Model. Simul.* **2019**, *11*, 69–83. [CrossRef]
8. Aashoor, F.A.O.; Robinson, F.V.P. Maximum power point tracking of photovoltaic water pumping system using fuzzy logic controller. In Proceedings of the 2013 48th International Universities' Power Engineering Conference (UPEC), Dublin, Ireland, 2–5 September 2013; pp. 1–5. [CrossRef]
9. Laabidi, H.; Mami, A. Grid connected Wind-Photovoltaic hybrid system. In Proceedings of the 2015 5th International Youth Conference on Energy (IYCE), Pisa, Italy, 27–30 May 2015; pp. 1–8.
10. El Hassouni, B.; Ourahou, M.; Ayrir, W.; Haddi, A.; Amrani, A.G. A Study of Efficient MPPT Techniques for Photovoltaic System Using Boost Converter. *Int. J. Emerg. Electr. Power Syst.* **2018**, *19*, 20170180. [CrossRef]
11. Mansouri, A.; El Magri, A.; Lajouad, R.; El Myasse, I.; Younes, E.K.; Giri, F. Wind energy based conversion topologies and maximum power point tracking: A comprehensive review and analysis. *e-Prime-Adv. Electr. Eng. Electron. Energy* **2023**, *6*, 100351. [CrossRef]
12. Kassem, A.M. Modeling, analysis and neural MPPT control design of a PV-generator powered dc motor-pump system. *WSEAS Trans. Syst. Arch.* **2011**, *10*, 399–412.
13. Asim, M.; Tariq, M.; Mallick, M.A.; Ashraf, I. An Improved Constant Voltage Based MPPT Technique for PMDC Motor. *Int. J. Power Electron. Drive Syst. (IJPEDS)* **2016**, *7*, 1330–1336. [CrossRef]
14. Sweidan, T.; Widyan, M.; Rifai, M. Perturbation and Observation as MPPT for Highly Penetrated Grid-Integrated PV Generator Considering Symmetrical Three-Phase Fault. *Int. J. Power Energy Convers.* **2019**, *10*, 225–240.
15. Abuashour, M.I.; Widyan, M.; Sweidan, T.O.; Almomani, M. Modeling, Simulations and Operational Performance of a Stand-Alone Hybrid Wind/PV Energy System Supplying Induction Motor for Pumping Applications. *Int. J. Eng. Syst. Model. Simul.* **2018**, *10*, 12–25.
16. Shukla, T.; Nikolovski, S. A Solar Photovoltaic Array and Grid Source-Fed Brushless DC Motor Drive for Water-Pumping Applications. *Energies* **2022**, *16*, 6133. [CrossRef]
17. Eswaraiah, B.; Balakrishna, K. Design and development of different adaptive MPPT controllers for renewable energy systems: A comprehensive analysis. *Sci. Rep.* **2024**, *14*, 21627. [CrossRef] [PubMed]
18. Fatah, A.; Boutabba, T.; Benlaloui, I.; Drid, S.; Mahmoud, M.M.; Hussein, M.M.; Mbasso, W.F.; Hussein, H.S.; Ewias, A.M. Design, and dynamic evaluation of a novel photovoltaic pumping system emulation with DS1104 hardware setup: Towards innovative in green energy systems. *PLoS ONE* **2024**, *19*, e0308212. [CrossRef] [PubMed]
19. Farhat, M.; Barambones, O. Advanced Control Scheme Optimization for Stand-Alone Photovoltaic Water Pumping Systems. *Computation* **2024**, *12*, 224. [CrossRef]
20. Al Mashhadany, Y.; Keream, S.S.; Algburi, S.; Alrawi, A.A.A. Analysis of High Performance of Separately Excited DC Motor Speed Control Based on Chopper Circuit. In Proceedings of the 2023 16th International Conference on Developments in eSystems Engineering (DeSE), Istanbul, Türkiye, 18–20 December 2023; pp. 19–23. [CrossRef]
21. Wubu, D.A.; Salau, A.O.; Alitasb, G.K. Particle Swarm Optimization Algorithm Based Fuzzy PID Controller Design for Speed Tracking Control of Separately Excited DC Motor. *Adv. Control Appl. Eng. Ind. Syst.* **2024**, e237. [CrossRef]
22. Sridhar, R.; Dhar, S. Performance analysis of a standalone PV system with reduced switch cascaded multilevel inverter. *Int. J. Power Energy Convers.* **2015**, *6*, 107–127. [CrossRef]
23. Patel, M.R. *Wind and Solar Power System*; CRC Press LLC: Abingdon, UK, 1999.
24. Ong, C.-M. *Dynamic Simulation of Electric Machinery: Using MATLAB/SIMULINK*; Prentice Hall PTR: Upper Saddle River, NJ, USA, 1998; p. 07458.
25. Jain, S.; Agarwal, V. Comparison of the performance of maximum power point tracking schemes applied to single-stage grid-connected photovoltaic systems. *Electr. Power Appl. IET* **2007**, *5*, 753–762. [CrossRef]
26. Mohan, N.; Undel, T.M. *Power Electronics: Converters, Applications, and Design*; John Wiley & Sons: Hoboken, NJ, USA, 2007.
27. Abu-Siada, A.; Islam, S.M. Chapter 23-Applications of Power Electronics in Renewable Energy Systems. In *Power Electronics Handbook*, 5th ed.; Rashid, M.H., Ed.; Butterworth-Heinemann: Oxford, UK, 2024; pp. 797–843.
28. Eldali, F. Chapter 30-Power Electronics for Distributed Energy. In *Power Electronics Handbook*, 5th ed.; Rashid, M.H., Ed.; Butterworth-Heinemann: Oxford, UK, 2024; pp. 977–992.
29. Kolhe, M.; Joshi, J.C.; Kothari, D.P. Performance analysis of a directly coupled photovoltaic water-pumping system. *IEEE Trans. Energy Convers.* **2004**, *19*, 613–618. [CrossRef]

30. Guerrero-Ramirez, E.; Martinez-Barbosa, A.; Contreras-Ordaz, M.A.; Guerrero-Ramirez, G.; Guzman-Ramirez, E.; Barahona-Avalos, J.L.; Adam-Medina, M. DC Motor Drive Powered by Solar Photovoltaic Energy: An FPGA-Based Active Disturbance Rejection Control Approach. *Energies* **2022**, *15*, 6595. [CrossRef]
31. Sorouri, H.; Sedighizadeh, M.; Oshnoei, A.; Khezri, R. An intelligent adaptive control of DC–DC power buck converters. *Int. J. Electr. Power Energy Syst.* **2022**, *141*, 108099. [CrossRef]
32. Mustafa, R.J.; Gomaa, M.R.; Al-Dhaifallah, M.; Rezk, H. Environmental Impacts on the Performance of Solar Photovoltaic Systems. *Sustainability* **2020**, *12*, 608. [CrossRef]
33. Raj, A.; Praveen, R. Highly efficient DC-DC boost converter implemented with improved MPPT algorithm for utility level photovoltaic applications. *Ain Shams Eng. J.* **2022**, *13*, 101617. [CrossRef]
34. Alkuhayli, A.; Noman, A.M.; Al-Shamma'a, A.A.; Abdurraqeeb, A.M.; Alharbi, M.; Hussein Farh, H.M.; Qamar, A. Enhancing Photovoltaic-Powered DC Shunt Motor Performance for Water Pumping Through Fuzzy Logic Optimization. *Machines* **2024**, *12*, 442. [CrossRef]